

The EBLM Project XVIII. 3D Obliquities of Five Low-Mass Eclipsing Binaries

Becca Spejcher^{1*}, David V. Martin¹, Jake Pandina¹, Andy Zhang¹, Max Ammons¹,
 Wata Tubthong¹, Amaury Triaud², Ritika Sethi³, Noah Vowell⁴, Adrian Barker⁵,
 Pierre Maxted⁶, Alison Duck^{8,7}, Shelby Summers⁷, François Bouchy⁹, Monika Lendl⁹,
 Maxime Marmier⁹, Vincent Megevand⁹, Francesco Pepe⁹, Malte Tewes¹⁰, Stéphane Udry⁹

¹*Department of Physics and Astronomy, Tufts University, Medford, MA 02155, USA*

²*School of Physics and Astronomy, University of Birmingham, Edgbaston, Birmingham B15 2TT, UK*

³*Department of Physics, Massachusetts Institute of Technology, Cambridge, MA 02139, USA*

⁴*Department of Physics and Astronomy, Michigan State University, East Lansing, MI 48824, USA*

⁵*School of Mathematics, University of Leeds, Leeds LS2 9JT, UK*

⁶*Astrophysics Group, Keele University, Keele, Staffordshire, ST5 5BG, UK*

⁷*Department of Astronomy, The Ohio State University, Columbus, OH 43210, USA*

⁸*Jet Propulsion Laboratory, California Institute of Technology, 4800 Oak Grove Drive, Pasadena, CA 91109, USA*

⁹*Observatoire Astronomique de l'Université de Genève, Chemin Pegasi 51, CH-1290 Versoix, Switzerland*

¹⁰*Universität Bonn, Argelander-Institut für Astronomie, Auf dem Hügel 71, 53121 Bonn, Germany*

Under Review (first submission November 2025)

ABSTRACT

A question that continues to perplex astronomers is the formation of tight stellar binaries. There is too much angular momentum in a collapsing and fragmenting protostellar cloud to form a stellar binary in situ with a separation less than an AU, yet thousands of these short-period binaries have been discovered. One indication of a binary's formation is the angle between the stellar spin and orbital axes — its obliquity. The classical method for determining projected stellar obliquity is the Rossiter-McLaughlin effect. This method has been applied to over 100 hot Jupiters, yet only a handful of stellar binaries. Of the binary systems with measured projected obliquities, even fewer have measured 3D obliquities. In this paper, we add five more short-period binary 3D obliquity measurements to the sample that previously consisted of a single system. We present Rossiter-McLaughlin measurements for EBLM J0239-20, EBLM J0941-31, EBLM 1037-25, EBLM 1141-37, and EBLM J2025-45. These systems consist of an M-dwarf eclipsing an F/G type primary. We combined CORALIE and HARPS spectroscopy with TESS photometry of primary and secondary eclipses. We show that even though the sky-projected obliquities seem to be aligned, there is modest but non-zero spin-orbit misalignment (ψ between 5 and 20°). Our primary stars straddle the Kraft break at $\sim 6250K$. Finally, we derive the M-dwarf masses and radii to precisions better than 3%. With the exception of EBLM J0941-31, each system has an inflated radius greater than 5σ from the expected radius from stellar models.

Key words: stars: binaries-eclipsing, low-mass, fundamental parameters; techniques: photometric, spectroscopic

1 INTRODUCTION

The origin of tight stellar binaries continues to perplex astronomers. Collapsing and fragmenting clouds have too much angular momentum to place two stars on a separation of a fraction of an AU (orbital periods of \sim days, [Tohline 2002](#); [Moe & Kratter 2018](#)), yet thousands of short-period main sequence binaries have been discovered ([Raghavan et al. 2010](#); [Prša et al. 2011](#); [Jayasinghe et al. 2018](#); [Prša et al. 2022](#); [Mowlavi et al. 2023](#)). One piece of the formation puzzle is the spin-orbit obliquity of the binary. This can be measured using the Rossiter-McLaughlin (RM) effect ([Rossiter 1924](#); [McLaughlin](#)

[1924](#); [Queloz et al. 2000a](#); [Triaud et al. 2017](#)). This spectroscopic effect can be seen when an object, like a planet or a secondary star, transits the primary star. This technique has been primarily applied to hot Jupiters, with over 100 RM measurements to date, revealing diverse orbits: coplanar, misaligned, polar, and even retrograde ([Winn et al. 2005](#); [Fabrycky & Tremaine 2007](#); [Triaud et al. 2010](#); [Albrecht et al. 2012](#); [Dawson & Johnson 2018](#); [Rice et al. 2022](#); [Rossi et al. 2025](#)). In contrast, only a handful of RM effects have been measured for stellar binaries. Furthermore, the RM effect alone only provides a *projected* spin-orbit obliquity. An independent measurement of the

stellar rotation rate is needed to determine the *true 3D* obliquity. The majority of obliquity measurements in the literature are only projected, not true obliquities.

In 2010, we created the EBLM (Eclipsing Binary Low Mass) survey (see review in [Maxted et al. 2023](#)). The sample consists of M-dwarfs ($\approx 0.08 - 0.6 M_{\odot}$) eclipsing more massive F/G/K dwarfs. These systems were discovered as “false positives” from the WASP transiting hot Jupiter survey. There are multiple goals for the EBLM project, one of which is increasing the number of precise obliquities of eclipsing binaries. So far, the EBLM project has published obliquities for WASP-30 (an eclipsing brown dwarf) & EBLM J1219-39 ([Triaud et al. 2013](#)), EBLM J0218-31 ([Gill et al. 2019](#)), the circumbinary planet host EBLM J0608-59 (also known as TOI-1338, BEBOP-1) ([Kunovac Hodžić et al. 2020](#)), and EBLM J0021-16 ([Spejcher et al. 2025](#)).

In this paper, we present RM measurements for five more EBLM systems: EBLM J0239-20, EBLM J0941-31, EBLM J1037-25, EBLM J1141-37, and EBLM J2025-45. The radial velocities both in and out-of-eclipse were observed with the CORALIE spectrograph. Additionally, EBLM J0941-31, EBLM J1037-25, and EBLM J1141-37 have out-of-eclipse radial velocities that were observed with the HARPS spectrograph. All five systems were observed by TESS, where photometry shows primary and secondary eclipses. For all five binaries, TESS photometry also reveals star spot modulation, from which we can derive the primary star’s rotation rate and hence determine a true 3D spin-orbit obliquity. Compared to 132 hot Jupiter obliquity measurements, only 8 eclipsing binaries have obliquity measurements. Even less-so, only one short-period eclipsing binary has had a true 3D obliquity measurement ([Spejcher et al. 2025](#)). Our sample adds five more sky-projected and true 3D obliquity measurements for short period eclipsing binaries, essentially quintupling the number of binaries with true 3D obliquity measurements.

Our paper is organized into the following sections: in Sect. 2 we describe the spectroscopic and photometric observations; in Sect. 3 we discuss our data-fitting methods; in Sect. 4 we discuss our results and in Sect. 5 we discuss implications of our results with respect to tidal physics, other measured obliquities in the literature, and M-dwarf radius inflation, followed by our conclusion.

2 OBSERVATIONS

2.1 CORALIE Radial Velocity Spectroscopy

The observational properties of the five EBLM systems are summarized in Table 1. The systems were first discovered photometrically by the Wide Angle Search for Planets (WASP) and were labeled as hot Jupiter candidates. Follow-up radial velocities (RVs, Fig. A1) were taken using the CORALIE spectrograph, which is a fiber-fed échelle spectrograph installed on the 1.2-m Leonard Euler telescope at the ESO La Silla Observatory, and has a resolving power of $R = 50,000 - 60,000$ ([Queloz et al. 2000b](#)). CORALIE has a wavelength range of 390 – 680 nm. It was quickly revealed that all five systems were not planets, but rather low mass eclipsing binaries, placing them into the EBLM program. Continued RVs were taken between March 2008 and November 2014 to map out the Keplerian orbit of the binary. In addition, each system received a sequence of spectroscopic measurements during the primary eclipse, yielding the RM effect. For EBLM J0239-20 the RM effect was observed on two separate occasions, owing to the relatively low signal to noise ratio of the effect. All RV data were processed using the standard CORALIE data

reduction pipeline ([Baranne et al. 1996](#)) using the cross-correlation method.

Three out of the five systems were also observed with the High Accuracy Radial velocity Planet Searcher (HARPS; [Mayor et al. 2003](#)) spectrograph on the 3.6m telescope at the ESO La Silla observatory as part of the Binaries Escorted By Orbiting Planets (BEBOP) survey for circumbinary planets. HARPS is a fiber-fed échelle spectrograph that uses a laser frequency comb to obtain an accuracy on the order of 1m/s. HARPS has a resolving power of $R = 115,000$ and covers the 378-691 nm wavelength range. The targets were observed at different times from April 2018 to December 2022; however, during this time, no eclipses were observed.

2.2 TESS Photometry

Each system has been observed by TESS for at least two sectors. The sectors during which they were observed are listed in Table 1. For all of the systems, we downloaded the PDCSAP (Pre-search Data Conditioned Simple Aperture Photometry) light curves via LIGHTKURVE ([Lightkurve Collaboration et al. 2018](#)). We downloaded the 120-second exposure time data that had been reduced through the SPOC (Science Processing Operations Center) pipeline. We chose to use the PDCSAP flux because it accounts for some instrumental effects, cosmic ray mitigation, and is corrected for dilution from nearby stars. We note that for our recent paper on the RM of EBLM J0021-16 ([Spejcher et al. 2025](#)) we used the SAP flux because the PDCSAP flux cut out a couple of eclipses and also had a detrending artefact that could be confused as the transit of a circumbinary planet. Such issues were not present in the five targets in this paper.

3 METHODS

3.1 Primary Star Parameters Using EXOFASTV2

The radius and effective temperature of the primary stars were constrained using EXOFASTV2 ([Eastman et al. 2019](#)) to fit a spectral energy distribution (SED) in combination with the MESA Isochrone and Stellar Tracks (MIST) model ([Dotter 2016](#)). This approach only applies the SED fitting and the MIST model to the FGK primary stars and not the eclipsing M-dwarf, whose properties are derived from transit fitting and the radial velocity measurements. The bolometric flux ratio between the primary and secondary stars is

$$\frac{F_B}{F_A} = \left(\frac{R_B}{R_A}\right)^2 \left(\frac{T_{\text{eff},B}}{T_{\text{eff},A}}\right)^4, \quad (1)$$

which for our stars ranges between 0.003 for EBLM J1141-37 and 0.0006 for EBLM J0239-20. Therefore, a single-star SED fit is reasonable in all cases for our sample since the eclipsing M-dwarf contributes well under 1% of the total flux.

The observed broadband photometric data are taken from Gaia DR3 ([Gaia Collaboration et al. 2022](#)), 2MASS ([Cutri et al. 2003](#)), and WISE ([Cutri et al. 2021](#)). We adopted priors on the primary star effective temperature and metallicity from [Freckelton et al. \(2024\)](#) as available for EBLM J0941-31, EBLM J1037-25, and EBLM J1141-37. We did not impose a stellar effective temperature or metallicity prior on EBLM J0239-20 and EBLM J1141-37. As the targets in our sample are a single-lined spectroscopic binaries, we cannot directly measure both stellar masses in a model-independent way. Thus, we use EXOFASTV2 to fit the MIST models ([Dotter 2016](#)) to estimate the primary star masses, as was done in previous EBLM work such as [Duck et al. \(2023\)](#).

Table 1. Summary of observational properties.

	EBLM J0239-20	EBLM J0941-31	EBLM J1037-25	EBLM J1141-37	EBLM J2025-45
TIC	64108432	25776767	187930369	454013359	369984032
TESS Sectors	4, 31	8, 9, 35, 62, 89	9, 36, 63, 89	10, 36, 37, 63, 90	27, 67
2MASS	J02392928-2002238	J09411676-3149102	J10370694-2534177	J11411219-3747297	J20252547-4549451
Gaia DR3 ID	5127259153974964480	5440085875822885888	5470783042175620992	5385134144388660352	6669738865254236928
RA (α) [BCRS]	02 ^h 39'29.29'' 39.872183856729855°	09 ^h 41'16.76'' 145.31970253162424°	10 ^h 37'06.94'' 159.2786174786457°	11 ^h 41'12.19'' 175.30046954074447°	20 ^h 25'25.48'' 306.35642054785717°
Dec (δ) [BCRS]	-20°02'23.99'' -20.04004991405048°	-31°49'10.31'' -31.819494031310178°	-25°34'17.73'' -25.57165320153576°	-37°47'29.62'' -37.791612660187354°	-45°49'45.16'' -45.82955952844853°
CORALIE Obs #	52	37	38	52	64
CORALIE Obs Δt [days]	1201	1839	1267	2176	1991
CORALIE Obs Date [UTC]	August 2009 - December 2012	March 2008 - March 2013	December 2009 - June 2013	August 2008 - July 2014	May 2009 - November 2014
CORALIE RM Obs Date [UTC]	November 11, 2009; December 19, 2009	February 14, 2010	March 10, 2010	April 24-25, 2010	September 7, 2010
HARPS Obs Date [UTC]		May 2018 - May 2022	May 2018 - March 2021	April 2018 - December 2022	
TESS-mag	10.1356 \pm 0.0081	10.638 \pm 0.006	9.6475 \pm 0.0062	8.995 \pm 0.006	10.3789 \pm 0.0061
B-mag	11.34 \pm 0.07	11.62 \pm 0.06	10.66 \pm 0.01	10.13 \pm 0.04	11.87 \pm 0.12
G-mag	10.568 \pm 0.003	11.039 \pm 0.003	10.020 \pm 0.003	9.397 \pm 0.003	10.892 \pm 0.003
V-mag	10.63 \pm 0.05	11.08 \pm 0.06	10.16 \pm 0.04	9.57 \pm 0.03	11.15 \pm 0.09
$G_{BP} - G_{RP}$	0.813	0.756	0.694	0.743	0.967
Parallax [mas]	3.867 \pm 0.0156	2.670 \pm 0.022	4.296 \pm 0.018	5.654 \pm 0.015	6.310 \pm 0.024
Distance [pc]	254.9135		231.2979	177.2652	157.1909
Gaia RUWE	0.94010013	1.2649149	0.9237525	0.99194455	1.2546798

3.2 Light Curve Detrending

We detrend the TESS light curves using the WOTAN (Hippke et al. 2019) Python package to remove any non-eclipse variability. This includes the effects of spot modulation on the primary star, gyroscopic movements from TESS, and scattered light by the Earth. For EBLM J0941-31, we applied a Tukey’s biweight filter with a window length of 0.6. For the other targets, we applied a spline with robust Huber-estimator with a break tolerance of 0.5. The window lengths chosen for these targets were calculated to be two times their eclipse duration.

3.3 Spectroscopy and Photometry Model Fit

3.3.1 PYMC3 and EXOPLANET

To determine the physical properties and orbital parameters of both stars in the binary, we use the EXOPLANET (Foreman-Mackey et al. 2021) package to model the eclipse light curves and RV profile, and employ the MCMC algorithm to derive the posterior of each property. EXOPLANET contains a suite of functionality that includes solving Kepler’s equation, Mandel & Agol (2002) light curves, quadratic limb darkening parameterization, and specialized impact parameter priors. Although originally developed for modeling stars with exoplanets, Foreman-Mackey et al. (2021) is applicable to eclipsing

binaries and has been used in past studies including Pass & Charbonneau (2023), Martin et al. (2024b,a), and Spejcher et al. (2025).

The PYMC3 package (Salvatier et al. 2016) is then used in conjunction with EXOPLANET to determine the best-fit parameters via the MCMC method. We use the built-in optimizer to find the *maximum a posteriori* (MAP) set of parameters and use it as the starting point of the MCMC sampling. The optimizer utilizes the Limited-memory Broyden–Fletcher–Goldfarb–Shanno (L-BFGS-B; Liu & Nocedal 1989) algorithm. The default fitting algorithm is the No-U-Turn Sampler (NUTS; Hoffman & Gelman 2011), which we use for all of our fits.

3.3.2 Fitting Keplerian RVs

We first perform a fit solely based on the Keplerian RV model, i.e. in-eclipse RVs were ignored. This is the same technique used in Spejcher et al. (under review). For EBLM J0941-31, EBLM J1037-25, and EBLM J1141-37, we simultaneously fit the RVs from CORALIE and HARPS. We fit the RV orbits with the following parameters: RV semi-amplitude (K), orbital period (P_{orb}), time of eclipse (T_0), eccentricity (e), the argument of periastron (ω), and systemic radial velocities (γ) – for the targets with HARPS and CORALIE observations, a separate parameter was fit for each dataset. Additionally, for EBLM J0239-20 and EBLM J0941-31, we fit a background radial velocity linear trend ($\dot{\gamma}$). This linear drift is likely due to a distant tertiary companion

orbiting these systems. We adopt the priors from [Triaud et al. \(2017\)](#) for the period and semi-amplitude. Priors for the time of eclipse and systemic background radial velocity were found by taking the median of the CORALIE observation times and the mean of the RV data, respectively. The time of eclipse, systematic background radial velocity, $\log(K)$, and $\log(P_{\text{orb}})$ were sampled using a normal distribution with a mean around their priors and a reasonable standard deviation. We sample over $\log(K)$ and $\log(P_{\text{orb}})$ instead of the semi-amplitude and period to more efficiently sample the parameter space. For e and ω , rather than sampling for these two parameters directly, we sample $h = \sqrt{e} \sin \omega$ and $k = \sqrt{e} \cos \omega$ to avoid introducing a biased estimate for e .

We use EXOPLANET to model the radial velocity of a Keplerian orbit. We then optimize the model parameters to find the MAP model and perform an MCMC with PYMC3. The resulting RV parameters from this model are then used as priors for the joint RV and photometry fit.

3.3.3 Joint RV and Photometry Fit

After getting the best-fit parameters from the Keplerian RV fit, we create a joint fit for the RV and photometry data sets. The posterior values from the RV fit are taken as priors for the parameters mentioned in Section 3.3.2. Additional parameters in the joint fit include the mass and radius of the primary star (M_A, R_A), the mass and radius of the secondary star (M_B, R_B), impact parameter (b), and quadratic limb darkening coefficients of both stars. To fit for the mass and radius of the primary star for EBLM J0239-20 and EBLM J0941-39, we use values from [Swayne et al. \(2024\)](#) as our priors. For EBLM J1037-25 and EBLM J1141-37, we use values from [Freckelton et al. \(2024\)](#) as our prior primary mass and radius values. For EBLM J2025-45, we used values from [Triaud et al. \(2017\)](#) as our primary mass and radius priors. The secondary star's mass and radius are calculated using the primary star's parameters, multiplied by the mass ratio ($q = M_A/M_B$) and radius ratio (R_B/R_A) respectively. The mass ratio is sampled on a logarithmic scale, while the radius ratio is sampled on a linear scale. We sample the impact parameter (b) using the built-in EXOPLANET function `xo.distributions.ImpactParameter`, which samples from a uniform distribution between zero to $1 + R_B/R_A$ ([Foreman-Mackey et al. 2021](#)).

The primary and secondary eclipse light curves are modeled using `xo.SecondaryEclipseLightCurve` from STARRY ([Luger et al. 2019](#)). The quadratic limb darkening coefficients are fitted using `xo.QuadLimbDark` function.

Similar to the RV fit, we optimize the starting parameters for MAP and then perform the MCMC sampling. We then use the posteriors from our joint fit as the priors to fit for the RM anomaly.

3.3.4 Secondary Star Effective Temperature

The depth of the secondary eclipse (Fig. A2) is indicative of the surface brightness ratio (S_B/S_A) between the two stars. This is not the same as the effective temperature ratio. Since we are only observing the eclipses in one photometric bandpass, and hence have no colour information, we have to be creative to estimate $T_{\text{eff},B}$. We follow the same procedure as done previously by [Swayne et al. \(2020, 2021\)](#); [Cañas et al. \(2022\)](#); [Duck et al. \(2023\)](#); [Spejcher et al. \(2025\)](#). The `xo.SecondaryEclipseLightCurve` function in our EXOPLANET/STARRY MCMC directly constrains the stellar radius ratio ($k = R_B/R_A$) and the secondary eclipse depth (D_{sec}). These are related to $T_{\text{eff},B}$ via

$$D_{\text{sec}} = k^2 S + A_g \left(\frac{R_B}{a} \right)^2, \quad (2)$$

$$= \left(\frac{R_B}{R_A} \right)^2 \frac{\int \tau(\lambda) F_{B,v}(\lambda, T_{\text{eff},B}) \lambda d\lambda}{\int \tau(\lambda) F_{A,v}(\lambda, T_{\text{eff},A}) \lambda d\lambda} + A_g \left(\frac{R_B}{a} \right)^2, \quad (3)$$

where A_g is the geometric albedo, $\tau(\lambda)$ ¹ is the TESS transmission function as a function of wavelength λ and F is the normalised flux. For eclipsing M-dwarfs, A_g is close enough to zero and the secondary star temperature is hot enough such that the second term of Eq. 3 can be ignored.

We calculate the integrated flux of the primary star using a high-resolution PHOENIX model spectrum, convolved with the TESS bandpass. The model spectrum is based on the best-fit values for $T_{\text{eff},A}$, $\log g_A$ and $[\text{Fe}/\text{H}]$ from EXOFASTv2. We then calculate the brightness of the secondary star across a grid of potential effective temperatures between 2300 and 4000 K. Using Brent minimisation we solve for $T_{\text{eff},B}$. This process is repeated with values of the radius ratio (R_B/R_A) and secondary eclipse depth (D_{sec}) randomly drawn from 1σ errors of the MCMC-fitted parameters. From this we derive a posterior and errorbar on $T_{\text{eff},B}$.

3.4 Fitting the Rossiter-McLaughlin Anomaly

We use the RM effect to measure the alignment between the stellar spin axis and the orbital axis in our systems. Since EBLM has a very uneven flux ratio ($F_B/F_A \sim 0.0015$), we are inherently referring to the spin-axis of the primary star. At its core, the RM effect is a distortion of stellar spectral lines during a transit or eclipse, caused by the foreground object (in our case, an M-dwarf) blocking rotating regions of the background star (F/G/K dwarf) and creating an asymmetric Doppler profile. Traditional methods for RM fitting constrain the projected rotational velocity of the occulted star, $v_{\text{rot}} \sin I_{\star}$, and the magnitude of the projected spin-orbit obliquity, $|\lambda|$. [Hirano et al. \(2011\)](#) updated RM models to account for macroturbulence (ζ), thermal broadening (β) and Lorentzian broadening (natural and pressure γ). We combine the [Gupta \(2024\)](#) publicly-available implementation of the [Hirano et al. \(2011\)](#) model into our EXOPLANET joint fit of the Keplerian RVs and photometric eclipses. This is similar to what [Carmichael et al. \(2025\)](#) used to fit the RM effect of brown dwarfs with EXOFASTv2 and is the same technique used in [Spejcher et al. \(2025\)](#). In Fig. 1 we show the fitted RM anomaly's of our systems.

The code from [Gupta \(2024\)](#) outputs the *sky-projected obliquity* (λ). This tells us how misaligned our system is as seen from Earth. For any system that has an observed RM anomaly, we can fit for λ . For most systems, this is the only obliquity that can be measured. However, if a star has a known rotational period, we can calculate the *true obliquity* (ψ) using the equation

$$\cos \psi \approx \cos \lambda \frac{P_{\text{rot}} v_{\text{rot}} \sin I_{\star}}{2\pi R_A}, \quad (4)$$

as is the case with our five EBLM targets. As seen in Fig. 2, λ is the angle between the sky projections of the orbital and rotational axes, where ψ is measured between the axes in three dimensions ([Albrecht et al. 2022](#)).

The stellar rotation period of each system's primary star was measured by [Sethi & Martin \(2024\)](#) using spot modulations. Since star

¹ <http://svo2.cab.inta-csic.es/svo/theory/fps3/index.php?id=Kepler/Kepler.K>

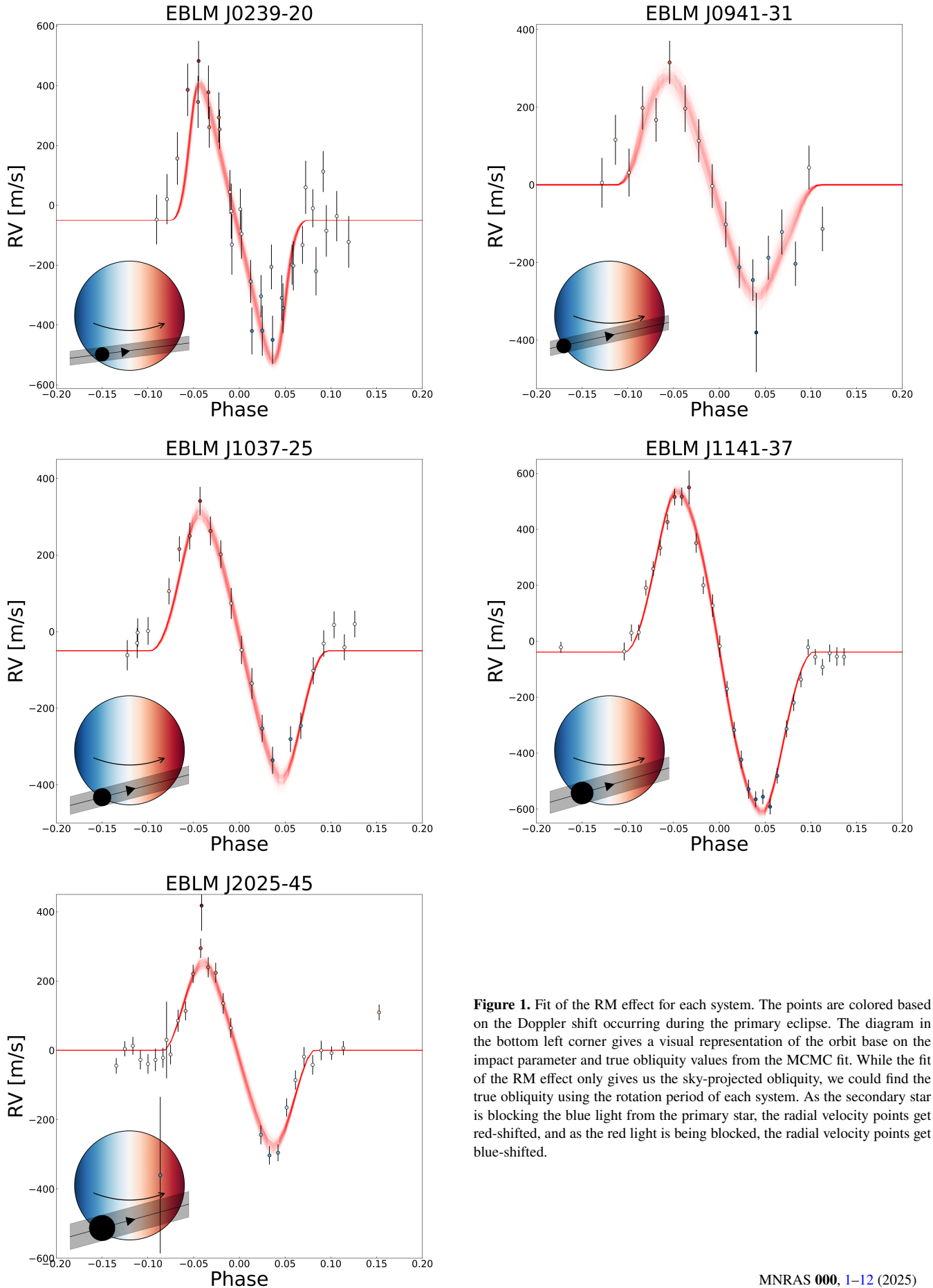


Figure 1. Fit of the RM effect for each system. The points are colored based on the Doppler shift occurring during the primary eclipse. The diagram in the bottom left corner gives a visual representation of the orbit base on the impact parameter and true obliquity values from the MCMC fit. While the fit of the RM effect only gives us the sky-projected obliquity, we could find the true obliquity using the rotation period of each system. As the secondary star is blocking the blue light from the primary star, the radial velocity points get red-shifted, and as the red light is being blocked, the radial velocity points get blue-shifted.

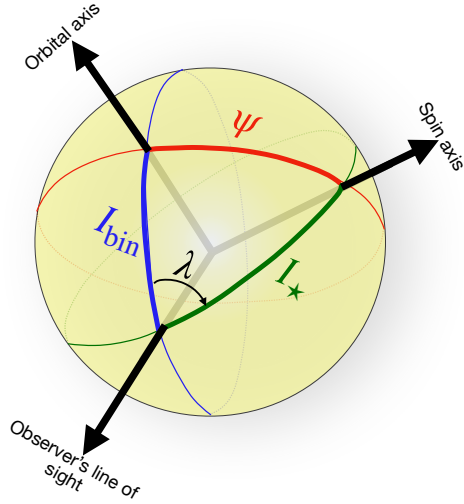


Figure 2. Orbital geometry of stellar obliquities adapted from a figure in [Albrecht et al. \(2022\)](#). The diagram shows ψ - the true stellar obliquity, λ - the sky-projected spin-orbit angle, I_* - the inclination of the rotation axis of the primary star, and I_{bin} - the orbital inclination of the binary.

spots are cooler and dimmer than the surrounding photosphere, the presence of a spot overdensity leads to periodic variations in brightness as the star rotates. By measuring the period of the out-of-eclipse variability in the TESS light curves, [Sethi & Martin \(2024\)](#) was able to determine the rotational periods of our systems, given in Table 3. We include this in our model as a Gaussian and use this to solve for the inclination. This will allow us to measure the true obliquity of the system using Eq. 4.

We use the Angle function from `PyMC3 EXTRAS` to find the best λ value within the range of $-\pi$ to π . This value is then fed into the Keplerian orbit model to fit the anomaly. We then use our fitted value for the rotation period to calculate the equatorial rotation velocity, where $v_{\text{rot}} = 2\pi R_A / P_{\text{rot}}$. With this we can find $\sin I_*$, where I_* is the stellar inclination, using the equation:

$$\sin I_* = \frac{v_{\text{rot}} \sin I_*}{v_{\text{rot}}} \quad (5)$$

With these parameters set, we then use Eq. 4 to calculate ψ as a deterministic variable. The final values for ψ and λ along with all the other parameters from the RM, RV, and photometry joint fit can be found in Table 3. The distributions of λ , ψ , P_{rot} , and $v_{\text{rot}} \sin I_*$ for each system can be found in Fig. A3 - A7.

4 RESULTS

Our best-fitted parameters for each system are shown in Table 3. Using the methods outlined in Section 3 for modeling the RM anomaly, we found each system to have a sky-projected obliquity of $|\lambda| < 5^\circ$, with the exception of EBLM J0941-31, which has a sky-projected obliquity of $|\lambda| = 11.7 \pm 4.8^\circ$. All systems have a measured true obliquity of $\psi < 20^\circ$. EBLM J0239-20 and EBLM J1141-37 have nearly circular orbits, where EBLM J0941-31, EBLM J1037-25, and EBLM 2025-45 have more eccentric orbits.

Table 2. Orbital period (P_{orb}), secondary mass (M_B), projected obliquity $|\lambda|$, and true obliquity (ψ , if measured) for all EBLM targets with measured RMs. This includes the brown dwarf WASP-30.

Target	P_{orb} [days]	M_B [M_\odot]	$ \lambda $ [$^\circ$]	ψ [$^\circ$]	Citation
WASP-30	4.156739 ± 0.000011	0.0597 ± 0.0011	7 \pm 23		Triaud et al. (2013)
EBLM J1219-39	6.7600098 ± 0.000028	0.0910 ± 0.0021	4.1 \pm 5		Triaud et al. (2013)
EBLM J0218-31	8.884102 ± 0.000011	0.390 ± 0.009	4 \pm 7		Gill et al. (2019)
EBLM J0608-59	14.608559 ± 0.000013	0.313 ± 0.011	2.8 ± 17.1		Kunovac Hodžić et al. (2020)
EBLM J0021-16	5.96727088 ± 0.00000034	0.1877 ± 0.0011	2.0 ± 1.1	28.9 ± 2.1	Spejcher et al. (2025)
EBLM J0239-20	2.77868784 ± 0.00000034	0.17416 ± 0.00092	4.2 ± 2.2	7.9 ± 1.2	Spejcher et al. (this work)
EBLM J0941-31	5.54564703 ± 0.00000045	0.2309 ± 0.0057	11.7 ± 4.8	15.5 ± 6.1	Spejcher et al. (this work)
EBLM J1037-25	4.93655905 ± 0.00000021	0.2755 ± 0.0013	2.64 ± 1.3	15.8 ± 5.5	Spejcher et al. (this work)
EBLM J1141-37	5.147689047 ± 0.000000099	0.3679 ± 0.0066	0.32 ± 0.69	23.6 ± 2.6	Spejcher et al. (this work)
EBLM J2025-45	6.19198051 ± 0.00000025	0.2239 ± 0.0014	0.7 ± 1.7	15.1 ± 6.8	Spejcher et al. (this work)

Note — [Triaud et al. \(2013\)](#) accounted for asymmetrical errors in their fits of WASP-30 and EBLM J1219-39, so the errors given here are the average of the asymmetric errors given in [Triaud et al. \(2013\)](#). This was done to provide a rough symmetry of errors to match the errors from our calculation, which assumes a 1σ symmetry.

5 DISCUSSION & CONCLUSION

5.1 Tidal Effects

For binary systems with sufficient angular momentum, tides act to bring the system to three equilibrium states ([Hut 1980](#); [Ogilvie 2014](#); [Barker 2025](#)):

- (i) spin-orbit alignment: the true obliquity $\psi = 0^\circ$;
- (ii) spin-orbit synchronization: the primary and secondary stellar rotation rate equals the orbital period, $P_{\text{rot}} = P_{\text{orb}}$;
- (iii) circularization: the orbital eccentricity $e = 0$.

In this paper, we measured five EBLM systems using a joint MCMC fit to measure the eccentricity and true obliquity of the systems. The true obliquity for each system shows slight spin-orbit misalignment, with $\psi \approx 15^\circ$. EBLM J0239-20 is an exception with $\psi = 7.9 \pm 1.2^\circ$. Note that we can only speak of the spin of the primary star for each system.

We use spin-orbit synchronization and circularization timescales from [Sethi et al. \(under review\)](#) for our systems. These values can

be found in the last rows of Table 3. Sethi et. al. (under review) used the methods in Barker (2020), given by:

$$\tau_{\text{sync}} = \frac{2Q' r_g^2}{9\pi} \left(\frac{M_A + M_B}{M_B} \right)^2 \frac{P_{\text{orb}}^4}{P_{\text{dyn}}^2 P_{\text{rot}}}, \quad (6)$$

where $P_{\text{dyn}} = 2\pi\sqrt{R_A^3/(GM_A)}$ is the dynamical timescale of the primary star and r_g^2 is its squared radius of gyration (see Barker 2020 for further details). Sethi et. al. (under review) represent Q' from the dissipation of inertial waves according to the frequency-averaged formalism of Ogilvie (2013). This accounts for the realistic structure of the star following Barker (2020, 2022). For solar-type main-sequence stars with masses less than $1.1M_{\odot}$, a typical value for Q' is $Q' \sim 10^7 (P_{\text{rot}}/10\text{d})^2$ and is the simplest way to represent inertial wave dissipation (see Lin & Ogilvie 2017, Barker 2020, and Sethi et. al. (under review)). Sethi et. al. (under review) uses this definition of Q' for all of the systems in their sample, including our systems.

Spin-orbit synchronization occurs when $P_{\text{orb}}/P_{\text{rot}} = 1$. Within 2σ of the rotational period of each system, EBLM J0239-20, EBLM J1037-25, and EBLM J1141-37 have synchronous orbits. This is in alignment with the calculated synchronization timescales from Sethi et al. (under review), who found the timescales for these systems to be between 10^5 and 10^7 years. EBLM J0941-31 is a supersynchronous system, with $P_{\text{orb}}/P_{\text{rot}} > 1$, and EBLM J2025-45 is a sub-synchronous system with $P_{\text{orb}}/P_{\text{rot}} < 1$. Both of these systems are almost synchronized, but $P_{\text{orb}}/P_{\text{rot}} \neq 1$ within 2σ of the rotational period. The timescales of synchronization for EBLM J0941-31 and EBLM J2025-45 are on the order of 10^7 and 10^6 years respectively, so we would expect these systems to be synchronized.

It is worth noting that the classical pseudo-synchronous rotation period for eccentric orbits with small e can be approximated by

$$P_{\text{rot,ps}} \approx \frac{P_{\text{orb}}}{1 + 6e^2} \quad (7)$$

For pseudo-synchronisation the rotation speed of the primary star is approximately equal to the orbital speed at periaapsis. For our three eccentric systems, we find that $P_{\text{rot,ps}} = 4.49$ for EBLM J0941-31, suggesting that the secondary is slowing down as it orbits the primary, which is consistent with pseudo-synchronization. EBLM J1137-25 has a pseudo-synchronous rotational period of $P_{\text{rot,ps}} = 4.54$, but has observed rotational and orbital periods that are consistent with full synchronization. And for EBLM J2025-45, we find a pseudo-synchronous rotational period of $P_{\text{rot,ps}} = 5.65$ compared to an observed rotational period of $P_{\text{rot}} = 6.43$ and an orbital period of $P_{\text{orb}} = 6.19$ days. This system is rotating slower than expected. We are hesitant to draw strong conclusions from a single system though, and note that differential rotation could confuse our observed rotation periods.

Sethi et. al. (under review) does not include timescales for spin-orbit alignment of our systems. However, from Lai (2012); Ogilvie (2014); Barker (2016, 2020), we can find the realignment time scale using:

$$\tau_{\psi} = \frac{4Q' r_g^2}{9\pi} \left(\frac{M_A + M_B}{M_B} \right)^2 \frac{P_{\text{orb}}^4}{P_{\text{dyn}}^2 P_{\text{rot}}} = 2\tau_{\text{sync}}, \quad (8)$$

assuming a similar Q' applies to damp obliquity tides as $l = m = 2$ tides. This is approximately the case by comparing Lin & Ogilvie (2017) with the corresponding $l = m = 2$ case.

The computed timescales for realignment for our sample range

from 10^5 to 10^7 years, which is smaller than the MIST stellar ages of all of the systems, which are on the order of 10^9 years. This suggests that all of our systems should be spin-orbit aligned.

Sethi et. al. (under review) calculated the circularization timescales for both circularization driven by primary dissipation and circularization driven by secondary dissipation using the equation given by Barker (2020):

$$\tau_{e,A} = \frac{2Q'}{63\pi} \left(\frac{M_A}{M_B} \right) \left(\frac{M_A + M_B}{M_A} \right)^{\frac{5}{3}} \frac{P_{\text{orb}}^{\frac{13}{3}}}{P_{\text{dyn}}^{\frac{10}{3}}}, \quad (9)$$

where P_{dyn} for the primary star is the same as defined previously. To calculate $\tau_{e,B}$, we can interchange subscripts A and B in Eq. 9 and compute P_{dyn} for the secondary star.

For each of our systems, the timescales for circularization driven by secondary dissipation was found to be more efficient than primary dissipation ($\tau_{e,B} \sim 10^5 - 10^6$ years versus $\tau_{e,A} \sim 10^8 - 10^9$ years). Additionally, all systems are expected to have circularized orbits if we take the minimum circularization timescale ($\tau_{e,B}$ in our case). Our sample contains two systems with nearly circular orbits (EBLM J0239-20, EBLM J1141-37), which is expected when taking both primary and secondary timescales from Sethi et. al. (under review). EBLM J1037-25 has circularization timescales of $\tau_{e,A} = 8.28 \times 10^8$ years and $\tau_{e,B} = 1.01 \times 10^6$ years, so we expect a circularized orbit. However, we measure the eccentricity of the system to have a modest eccentricity of $e = 0.12139 \pm 0.000075$. Although all systems are expected to be circularized based off the secondary dissipation circularization timescales, EBLM J0941-31 and EBLM J2025-45 are expected to still be going through tidal circularization based on the circularization timescales driven by primary dissipation. This is consistent with our measured eccentricities of these systems ($e > 0.1$, see Sethi et. al. (under review) for further details).

5.2 Obliquity Across the Spectrum of Mass Ratio

Table 2 shows the orbital period (P_{orb}), secondary mass (M_B), sky-projected obliquity $|\lambda|$, and true obliquity (ψ) for each EBLM system with a measured RM, including the brown dwarf WASP-30 and the 5 systems discussed in this work. Note that the only other stellar binary with a measured true obliquity before this work is EBLM J0021-16 from Spejcher et al. (2025).

In Fig. 3, we show the projected and true obliquities for all giant planets, brown dwarfs, and stellar companions with $M_b > 0.7$ (Southworth 2011; Marcussen & Albrecht 2022; Carmichael et al. 2025; Vowell et al. 2025). Smaller mass ratios, concentrated around $q = 10^{-3}$, correspond to RM measurements of hot Jupiters. We can see that roughly 1/3 of the hot Jupiter population is misaligned (Triaud et al. 2010; Winn & Fabrycky 2015). Note that a majority of the misaligned hot Jupiter's have primary star temperatures greater than the Kraft break (~ 6250 K; Kraft 1967). This is likely because stars above the Kraft break have radiative outer envelopes, which is thought to be less efficient for tidal realignment. Hot Jupiters with primary stars below the Kraft break tend to be more aligned, which corresponds to stars with thick convective outer envelopes and more efficient tidal effects. Another trend that emerges when looking at the obliquity of systems with different mass ratios is that systems with larger mass ratios tend to be more aligned (Rusznak et al. 2025; Carmichael et al. 2025; Vowell et al. 2025). This is likely due to tides being more efficient in systems with higher mass ratios. This can be seen in Eq. 8, which shows that the realignment timescale for stars with convective envelopes scale as $\tau_{\text{align,CE}} \propto 1/q^2$, which suggests eclipsing binaries (high q) might all be aligned. Zahn (1977) also

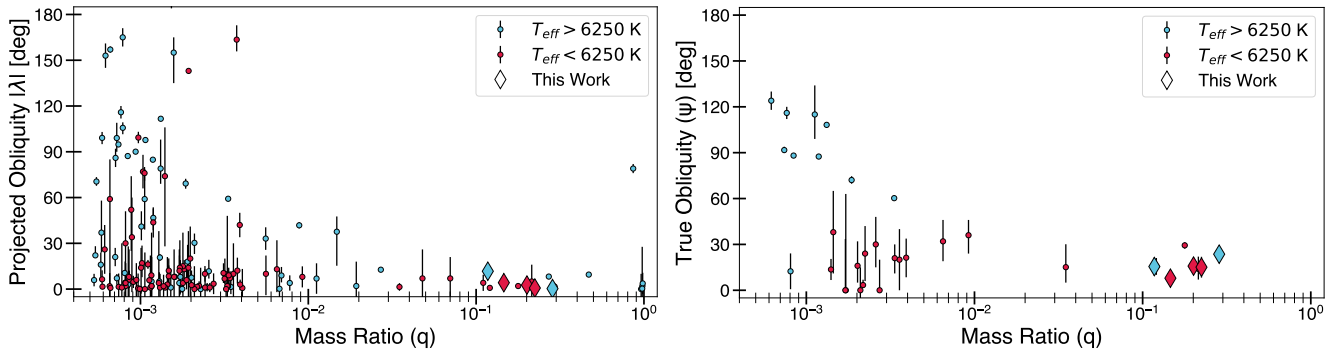


Figure 3. Sky-projected stellar obliquity $|\lambda|$ vs. mass ratio (q , left) and true 3-D Stellar Obliquities (ψ) vs mass ratio (right) for eclipsing companions, $M_b > 0.7 M_J$. Obliquities measured via apsidal motion are not depicted. Red points depict systems with primary stars below the Kraft break (~ 6250 K; Kraft 1967), and blue points depict those above. The new systems we add are shown as diamonds. The giant planet and brown dwarf obliquities were retrieved from TEPcat (Southworth 2011) and Carmichael et al. (2025); Vowell et al. (2025). The eclipsing binary obliquities are from Marcussen & Albrecht (2022); Spejcher et al. (2025); Wells et al. (2025).

shows that there is an even stronger relationship between alignment timescales and mass ratio for hotter stars, with radiative outer envelopes. For systems with host stars above $1.6M_\odot$, the realignment timescale scales as $\tau_{\text{align,RE}} \propto 1/(q^2(1+q)^{5/6})$.

It is important to note that we define the Kraft break to be $T_{\text{eff}} = 6250\text{K}$, which is consistent with traditional obliquity studies. A recent paper by Wang et al. (2025) shows that if you consider obliquity measurements for single star systems only, the obliquity transition between aligned and misaligned systems moves closer to $\sim 6500\text{K}$, which is more consistent with the rotational Kraft break. However, if you consider single star *and* multiple star systems with obliquity measurements, you find the obliquity transitions sits at the traditional 6250K value that we are using. In our sample, EBLM J0941-31A and EBLM J1141-37A both have effective temperatures greater than the traditional Kraft break ($T_A = 6450\text{K}$ and $T_A = 6390\text{K}$, respectively). The measured true 3D obliquities for these systems are both slightly misaligned. Our other 3 systems have primary effective temperatures under the Kraft break. Additionally, when Wang et al. (2025) describes single star systems, they are referring to just one object transiting a primary star. A multiple star system describes an object transiting a primary star with a long-period secondary stellar companion that is also orbiting the primary star. For our sample, a single star system is equivalent to our short-period eclipsing binaries with no known tertiary body compared to our short-period eclipsing binaries *with* a tertiary body. EBLM J0239-20 and EBLM J0941-31 both have a linear trend, indicative of a tertiary body. EBLM J0239-20 has a primary effective temperature below the Kraft break and is our most aligned system in our sample. EBLM J0941-31 has a primary effective temperature above the Kraft break and is expected to be misaligned in the context of Wang et al. (2025), however we only see slight misalignment.

We encourage caution with respect to interpreting these early measurements of tight stellar binary obliquities. Understanding how these binaries form and evolve will be an interesting challenge for more complex tidal models to describe the misalignment trends that we see here. More RM measurements, especially for more systems above the Kraft break and for longer period binaries, where tidal effects are slower, will shed more light on misalignment timescales.

5.3 Mass-Radius Relationship

Another of the EBLM survey is the precise characterization of M-dwarfs in eclipsing binaries (Maxted et al. 2023). The goal is to measure their mass and radius to a precision of better than a couple of per cent. More precisely-measured M-dwarf parameters are crucial to our understanding of stellar structure and evolution models. Furthermore, the reliability of our planetary parameters is dependent on the reliability of the stellar parameters. This requires better M-dwarf models, both theoretical and empirical.

We measure the mass and radius of our systems to less-than 3% uncertainties. It is important to note that these are nominal uncertainties and that the true uncertainties could be larger due to unaccounted for systematics. One source of systematic uncertainty comes from our derivation of primary star parameters. Since each system is a single-lined spectroscopic binary, we do not get model independent masses. However, Duck et al. (2023) showed for two EBLM systems that systematic model uncertainty can be similar to the nominal uncertainty.

Fig. 4 shows the distribution of mass and radius of the well-characterized M-dwarf population. The mass-radius relationship obtained from the MIST stellar model with $[\text{Fe}/\text{H}] = 0.0$ is also shown. Among this population, many M-dwarfs are observed to have larger radii than what was expected from the model. This was dubbed the “radius inflation” problem Parsons et al. (2018); Morrell & Naylor (2019). The secondary stars in our sample are shown by the black markers, each of which lie above the theoretical prediction. To quantify the radius inflation, we use the following equation from Gill et al. (2019):

$$\frac{\Delta R_B}{R_B} = \frac{R_B - R_{B,\text{exp}}}{R_B}, \quad (10)$$

where R_B is the radius of the M-dwarf given by the MCMC fit and $R_{B,\text{exp}}$ is the expected radius value from the MIST model. To find the expected radii of our systems, we interpolate over the MIST model using the mass of the M-dwarfs given by the MCMC joint fit (see Table 3). Fig. 4 (right) shows where each of our systems lie with respect to the MIST stellar model. It is clear that each system except for EBLM J0941-31B lies well above the model. These systems are all inflated by greater than 5σ from their expected radius values. EBLM J0941-31B is not inflated, as it is within 1σ from the expected radius value based on the MIST stellar model.

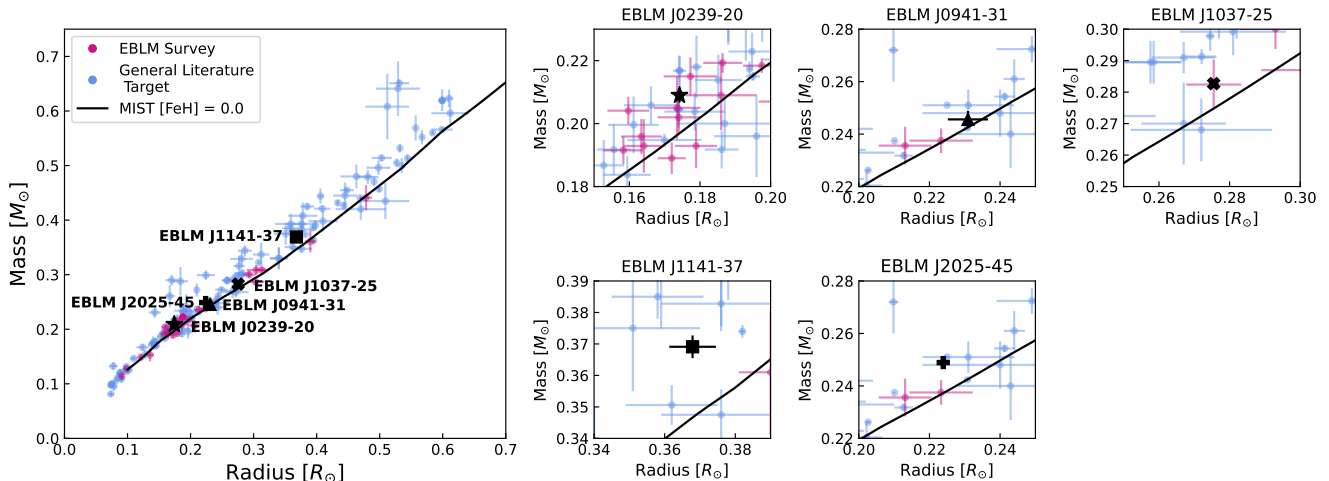


Figure 4. Mass vs. Radius plot for high-precision M-dwarfs, with data taken from Maxted et al. (2023). The plot includes targets from the EBLM survey (pink dots) and general literature targets (blue dots). Only targets with a mass or radius better than 10% are included here. The solid line passing through the data points indicates the MIST stellar model for $[\text{Fe}/\text{H}] = 0.0$. Our systems are highlighted by the black markers.

6 CONCLUSION

We combined CORALIE and HARPS spectroscopic data with TESS photometry to characterize a sample of five EBLM systems. Within our CORALIE RVs contain observations during primary eclipses for the systems. Additionally, TESS photometry shows strong star spot modulation, making it possible to measure the rotation period of the primary star in each system (Sethi & Martin 2024). This combination makes it possible to precisely characterize the Rossiter-McLaughlin effect in these systems, both the sky-projected and true 3D obliquity. We reveal that whilst the sky-projected obliquity for three systems suggests spin-orbit alignment ($\lambda < 3^\circ$), the true 3D obliquity tends to be slightly misaligned ($\psi > 15^\circ$). For EBLM J0239-20, we measure a sky-projected obliquity of $\lambda = 4.2 \pm 2.2^\circ$ and 3D obliquity of $\psi = 7.9 \pm 1.2^\circ$. For EBLM J0941-31, we measure a sky-projected obliquity of $\lambda = 11.7 \pm 4.8^\circ$ and a 3D obliquity of $\psi = 15.5 \pm 6.1^\circ$. Both of these systems have 3D obliquities that are more consistent with their sky-projected obliquities. It is interesting to note that both of these systems have a possible tertiary companion based on a necessary linear trend that needed to be added to their joint RV and photometry fits. Additionally, EBLM J0239-20 has a primary effective temperature below the Kraft break ($\sim 6250\text{K}$), has a nearly circular orbit ($e = 0.00198 \pm 0.00056$), and tends to be more aligned than EBLM J0941-31, which has a primary effective temperature above the Kraft break and a more elliptical orbit ($e = 0.19852 \pm 0.00013$).

Prior to this work, only five EBLM systems have measured sky-projected obliquities, and only one with a measured 3D obliquity (Spejcher et al. 2025). We have now doubled the number of EBLM systems with measured RM anomalies and quintupled the number of systems with measured true 3D obliquities. In total, there are now 13 main sequence eclipsing binaries with RM observations and measured sky-projected obliquities that show a majority are (or are close to being) spin-orbit aligned. This is in contrast to the 132 giant planets that have RM measurements and show a diversity of obliquities. Additionally, brown dwarf obliquity measurements show a similar alignment trend as short period stellar binaries. This may be due to tidal realignment in hot Jupiters being less efficient in systems with high mass ratios. Alternatively, we find that although the sky-

projected obliquities show near alignment for most of our systems, the true 3D obliquities show a slight misalignment. Our sample also provides two systems with primary effective temperatures above the Kraft break, both of which are slightly misaligned. This is expected to be a consequence of tidal realignment being less effective in stars with radiative outer envelopes. It is possible that more massive companions like brown dwarfs and M-dwarfs tend to be more aligned because they migrate differently than hot Jupiters (e.g. disk migration vs. high eccentricity tidal migration). To distinguish between whether more efficient tides or a difference in migration causes alignment for systems with higher mass ratios, we encourage further RM observations, particularly for eclipsing binaries with longer periods and hotter primary stars, where tides are expected to be weaker.

Finally, we measure the mass and radius of the M-dwarfs in our sample to a precision better than 3%. Comparing these values to the MIST stellar model with $[\text{Fe}/\text{H}] = 0.0$, we find that 4 out of 5 M-dwarfs have radii inflated by greater than 5σ . The exception to this is EBLM J0941-31, which has a radius that lies within 1σ from the expected value. This precise M-dwarf radius measurements add five more pieces to the radius inflation puzzle.

ACKNOWLEDGEMENTS

The EBLM Program has been supported by NASA TESS Guest Investigator Program through Cycle 1 (G011278), Cycle 2 (G022253), Cycle 3 (G03195), Cycle 4 (G04157), Cycle 5 (G05073), Cycle 6 (G06022), Cycle 7 (G07005) and Cycle 8. Postage stamp observations were provided in all 7 cycles and funding was provided in cycles 2, 4, 5 and 7. This research is also supported work funded from the European Research Council (ERC) the European Union’s Horizon 2020 research and innovation programme (grant agreement no803193/BEBOP). AJB was supported by STFC grants ST/W000873/1 and UKRI1179.

This paper is the result of work stemming from the AST-192 Research For Credit class in Spring 2025.

The authors would like to attract attention on the help and kind attention of the ESO staff at La Silla and on the dedication of the many technicians and observers from the University of Geneva, to

upkeep the telescope and acquire the data that we present here. We would also like to acknowledge that the Euler Swiss Telescope at La Silla is a project funded by the Swiss National Science Foundation (SNSF).

DATA AVAILABILITY STATEMENT

All radial velocities and light curves will be made available online.

REFERENCES

- Albrecht S., et al., 2012, *ApJ*, **757**, 18
- Albrecht S. H., Marcussen M. L., Winn J., Dawson R., Knudstrup E., 2022, in *Bulletin of the American Astronomical Society*, p. 501-05
- Baranne A., et al., 1996, *A&AS*, **119**, 373
- Barker A. J., 2016, *MNRAS*, **460**, 2339
- Barker A. J., 2020, *MNRAS*, **498**, 2270
- Barker A. J., 2022, *ApJ*, **927**, L36
- Barker A. J., 2025, *arXiv e-prints*, p. [arXiv:2504.10941](https://arxiv.org/abs/2504.10941)
- Cañas C. I., et al., 2022, *AJ*, **163**, 89
- Carmichael T. W., et al., 2025, *arXiv e-prints*, p. [arXiv:2506.18971](https://arxiv.org/abs/2506.18971)
- Cutri R. M., et al., 2003, *VizieR Online Data Catalog*, p. II/246
- Cutri R. M., et al., 2021, *VizieR Online Data Catalog*, p. II/328
- Dawson R. I., Johnson J. A., 2018, *ARA&A*, **56**, 175
- Dotter A., 2016, *ApJS*, **222**, 8
- Duck A., et al., 2023, *MNRAS*, **521**, 6305
- Eastman J. D., et al., 2019, EXOFASTv2: A public, generalized, publication-quality exoplanet modeling code ([arXiv:1907.09480](https://arxiv.org/abs/1907.09480)), <https://arxiv.org/abs/1907.09480>
- Fabrycky D., Tremaine S., 2007, *ApJ*, **669**, 1298
- Foreman-Mackey D., et al., 2021, *arXiv e-prints*, p. [arXiv:2105.01994](https://arxiv.org/abs/2105.01994)
- Freckelton A. V., et al., 2024, *MNRAS*, **531**, 4085
- Gaia Collaboration et al., 2022, *arXiv e-prints*, p. [arXiv:2208.00211](https://arxiv.org/abs/2208.00211)
- Gill S., et al., 2019, *A&A*, **626**, A119
- Gupta A. F., 2024, *Orbit Fitting (Transit + Radial Velocity + Rossiter-McLaughlin)*, <https://www.codeocean.com/doi:10.24433/CO.1015433.v1>
- Hippke M., David T. J., Mulders G. D., Heller R., 2019, *AJ*, **158**, 143
- Hirano T., Suto Y., Winn J. N., Taruya A., Narita N., Albrecht S., Sato B., 2011, *ApJ*, **742**, 69
- Hoffman M. D., Gelman A., 2011, *arXiv:1111.4246*
- Hut P., 1980, *A&A*, **92**, 167
- Jayasinghe T., et al., 2018, *MNRAS*, **477**, 3145
- Kraft R. P., 1967, *ApJ*, **150**, 551
- Kunovac Hodžić V., et al., 2020, *MNRAS*, **497**, 1627
- Lai D., 2012, *MNRAS*, **423**, 486
- Lightkurve Collaboration et al., 2018, *Lightkurve: Kepler and TESS time series analysis in Python*, *Astrophysics Source Code Library* (ascl:1812.013)
- Lin Y., Ogilvie G. I., 2017, *MNRAS*, **468**, 1387
- Liu D. C., Nocedal J., 1989, *Mathematical Programming*, **45**, 503–528
- Luger R., Agol E., Foreman-Mackey D., Fleming D. P., Lustig-Yaeger J., Deitrick R., 2019, *AJ*, **157**, 64
- Mandel K., Agol E., 2002, *ApJ*, **580**, L171
- Marcussen M. L., Albrecht S. H., 2022, *ApJ*, **933**, 227
- Martin D. V., Sethi R., Armitage T., Gilbert G. J., Rodríguez Martínez R., Gilbert E. A., 2024a, *MNRAS*, **528**, 963
- Martin D. V., et al., 2024b, *MNRAS*, **535**, 3343
- Maxted P. F. L., Triaud A. H. M. J., Martin D. V., 2023, *Universe*, **9**, 498
- Mayor M., et al., 2003, *The Messenger*, **114**, 20
- McLaughlin D. B., 1924, *ApJ*, **60**, 22
- Moe M., Kratter K. M., 2018, *ApJ*, **854**, 44
- Morrell S., Naylor T., 2019, *MNRAS*, **489**, 2615
- Mowlavi N., et al., 2023, *A&A*, **674**, A16
- Ogilvie G. I., 2013, *MNRAS*, **429**, 613
- Ogilvie G. I., 2014, *ARA&A*, **52**, 171
- Parsons S. G., et al., 2018, *MNRAS*, **481**, 1083
- Pass E. K., Charbonneau D., 2023, *ApJ*, **949**, 37
- Prša A., et al., 2011, *AJ*, **141**, 83
- Prša A., et al., 2022, *ApJS*, **258**, 16
- Queloz D., Eggenberger A., Mayor M., Perrier C., Beuzit J. L., Naef D., Sivan J. P., Udry S., 2000a, *Detection of a spectroscopic transit by the planet orbiting the star HD209458* ([arXiv:astro-ph/0006213](https://arxiv.org/abs/astro-ph/0006213)), <https://arxiv.org/abs/astro-ph/0006213>
- Queloz D., et al., 2000b, *A&A*, **354**, 99
- Raghavan D., et al., 2010, *ApJS*, **190**, 1
- Rice M., Wang S., Laughlin G., 2022, *ApJ*, **926**, L17
- Rossi A. M., Rainer M., Borsa F., Facchini S., 2025, *arXiv e-prints*, p. [arXiv:2511.10313](https://arxiv.org/abs/2511.10313)
- Rossiter R. A., 1924, *ApJ*, **60**, 15
- Rusznak J., Wang X.-Y., Rice M., Wang S., 2025, *ApJ*, **983**, L42
- Salvatier J., Wiecki T. V., Fonnesbeck C., 2016, *PeerJ Computer Science*, **2**, e55
- Sethi R., Martin D. V., 2024, *MNRAS*, **529**, 4442
- Southworth J., 2011, *MNRAS*, **417**, 2166
- Spejcher B., et al., 2025, *arXiv e-prints*, p. [arXiv:2509.21517](https://arxiv.org/abs/2509.21517)
- Swayne M. I., Maxted P. F. L., Hodžić V. K., Triaud A. H. M. J., 2020, *MNRAS*, **498**, L15
- Swayne M. I., et al., 2021, *MNRAS*, **506**, 306
- Swayne M. I., et al., 2024, *MNRAS*, **528**, 5703
- Tohline J. E., 2002, *ARA&A*, **40**, 349
- Triaud A. H. M. J., et al., 2010, *A&A*, **524**, A25
- Triaud A. H. M. J., et al., 2013, *A&A*, **549**, A18
- Triaud A. H. M. J., et al., 2017, *A&A*, **608**, A129
- Vowell N., et al., 2025, *arXiv e-prints*, p. [arXiv:2510.00105](https://arxiv.org/abs/2510.00105)
- Wang X.-Y., Wang S., Ong J. M. J., 2025, *arXiv e-prints*, p. [arXiv:2511.15610](https://arxiv.org/abs/2511.15610)
- Wells T., et al., 2025, *MNRAS*, **542**, 2269
- Winn J. N., Fabrycky D. C., 2015, *ARA&A*, **53**, 409
- Winn J. N., et al., 2005, *ApJ*, **631**, 1215
- Zahn J. P., 1977, *A&A*, **57**, 383

APPENDIX A: RV, PHOTOMETRY, AND CORNER PLOTS

Table 3. Final fitted parameter values for the joint Keplerian, RM, and photometric fit of EBLM J0021-16. For each fitted parameter, we include the prior values and their distribution that we ran in the code. We also include the timescales for synchronization and circularization as calculated in Sethi et al. (in prep) using Eq. 6 and 9 respectively. The realignment timescale was calculated using Eq. 8 from Barker (2016). The parameters are separated by physical, observable, and RM-specific parameters.

Parameter	Description	EBLM J0239-20	EBLM J0941-31	EBLM J1037-25	EBLM J1141-37	EBLM J2025-45
Physical Parameters						
$m_A (M_\odot)$	Primary Mass	$1.1908^{+0.0098}_{-0.0099}$	$1.1672^{+0.059}_{-0.056}$	$1.3721^{+0.01}_{-0.01}$	$1.2929^{+0.039}_{-0.038}$	$1.0011^{+0.01}_{-0.01}$
$m_B (M_\odot)$	Secondary Mass	$0.17416^{+0.00092}_{-0.00093}$	$0.21547^{+0.0068}_{-0.0064}$	$0.2755^{+0.0013}_{-0.0013}$	$0.36836^{+0.0068}_{-0.0066}$	$0.22399^{+0.0014}_{-0.0014}$
q	Mass Ratio	$0.14626^{+0.00045}_{-0.00047}$	$0.18478^{+0.0033}_{-0.0035}$	$0.20079^{+0.00055}_{-0.00055}$	$0.28502^{+0.0033}_{-0.0034}$	$0.22375^{+0.00084}_{-0.00087}$
$R_A (R_\odot)$	Primary Radius	$1.635^{+0.014}_{-0.014}$	$1.766^{+0.029}_{-0.027}$	$1.722^{+0.0071}_{-0.0077}$	$1.806^{+0.017}_{-0.016}$	$1.053^{+0.005}_{-0.0053}$
$R_B (R_\odot)$	Secondary Radius	$0.2092^{+0.0024}_{-0.0023}$	$0.2359^{+0.0042}_{-0.0039}$	$0.2827^{+0.0012}_{-0.0012}$	$0.3693^{+0.0034}_{-0.0033}$	$0.2491^{+0.0013}_{-0.0012}$
R_B/R_A	Radius Ratio	$0.12794^{+0.00064}_{-0.00063}$	$0.13362^{+0.00041}_{-0.00041}$	$0.16419^{+0.0008}_{-0.00075}$	$0.20446^{+0.00035}_{-0.00037}$	$0.23658^{+0.00098}_{-0.001}$
S_B/S_A	Surface Brightness Ratio	$0.02375^{+0.0018}_{-0.0018}$	$0.04121^{+0.0016}_{-0.0016}$	$0.05141^{+0.00083}_{-0.00085}$	$0.07156^{+0.00038}_{-0.00038}$	$0.06839^{+0.0012}_{-0.0012}$
$\rho (g/cm^3)$	Stellar Density	$0.3832^{+0.0089}_{-0.009}$	$0.298^{+0.0062}_{-0.0061}$	$0.378^{+0.004}_{-0.0039}$	$0.3084^{+0.0017}_{-0.0016}$	$1.206^{+0.014}_{-0.013}$
$T_A (K)$	Primary T_{eff}	5880 ± 150	6450 ± 120	5807 ± 78	6390 ± 245	5430 ± 115
$T_B (K)$	Secondary T_{eff}	2672 ± 52	3090 ± 38	3026 ± 26	3340 ± 78	3055 ± 43
Orbital Parameters						
t_0 (Days)	Time of Eclipse	$-1815.37339^{+0.00043}_{-0.00043}$	$4526.33509^{+0.00043}_{-0.00041}$	$5265.69871^{+0.00018}_{-0.0002}$	$8544.39821^{+2.7e-05}_{-2.6e-05}$	$-1553.31864^{+0.00026}_{-0.00026}$
P_{orb} (Days)	Orbital Period	$2.77868783^{+0.0000033}_{-0.0000032}$	$5.54564705^{+0.0000045}_{-0.0000047}$	$4.93655905^{+0.0000021}_{-0.0000020}$	$5.147689048^{+0.00000099}_{-0.00000099}$	$6.19197794^{+0.0000040}_{-0.0000040}$
b	Impact Parameter	$0.6382^{+0.01014}_{-0.01012}$	$0.36294^{+0.01962}_{-0.01928}$	$0.73196^{+0.002657}_{-0.002758}$	$0.63797^{+0.001369}_{-0.001372}$	$0.64393^{+0.005063}_{-0.005239}$
e	Eccentricity	$0.00199^{+0.00054}_{-0.00051}$	$0.19853^{+0.00014}_{-0.00014}$	$0.121398^{+0.000074}_{-0.000072}$	$0.000756^{+0.000048}_{-0.000048}$	$0.12651^{+0.00017}_{-0.00016}$
ω ($^\circ$)	Argument of Periastron	$-2.1476^{+0.086}_{-0.64}$	$0.097908^{+0.00096}_{-0.00096}$	$-1.2724^{+0.00033}_{-0.00034}$	$1.7221^{+0.033}_{-0.035}$	$-1.3544^{+0.00069}_{-0.00067}$
$r v_0$ (km/s)	Background	$19.3553030^{+0.0000099}_{-0.0000099}$	$4.15^{+0.061}_{-0.060}$	$28.9561^{+0.0061}_{-0.0060}$	$28.0391^{+0.0037}_{-0.0038}$	$-48.015684^{+0.000098}_{-0.000098}$
$\dot{\gamma}$	Linear Trend (km/s)	$0.0001580^{+0.0000061}_{-0.0000060}$	$-0.000010^{+0.000011}_{-0.000012}$			
I ($^\circ$)	Inclination	$1.4576^{+0.0026}_{-0.0026}$				
$a (R_\odot)$	Semi-major Axis	$9.226^{+0.024}_{-0.024}$	$14.68^{+0.23}_{-0.22}$	$14.41^{+0.033}_{-0.033}$	$14.86^{+0.14}_{-0.13}$	$15.18^{+0.048}_{-0.047}$
a (AU)	Semi-major Axis	$0.04291^{0.00011}_{-0.00011}$	$0.06829^{0.0011}_{-0.001}$	$0.06701^{0.00015}_{-0.00015}$	$0.0691^{0.00064}_{-0.00062}$	$0.07061^{0.00022}_{-0.00022}$
RM Parameters						
$v \sin I$ (km/s)	Projected Rotational Velocity	$31.61^{+0.47}_{-0.47}$	$17.25^{+0.89}_{-0.89}$	$16.54^{+0.54}_{-0.52}$	$16.32^{+0.28}_{-0.29}$	$7.83^{+0.28}_{-0.29}$
$ \lambda $ ($^\circ$)	Sky-Projected Obliquity	$4.3^{+2.1}_{-2.1}$	$12.0^{+4.9}_{-5.1}$	$2.7^{+1.3}_{-1.2}$	$0.31^{+0.71}_{-0.71}$	$3.3^{+1.9}_{-1.9}$
ψ ($^\circ$)	True Obliquity	$7.9^{+1.2}_{-1.1}$	$13.6^{+5.4}_{-5.3}$	$16.5^{+4.7}_{-6.3}$	$18.0^{+4.1}_{-5.2}$	$17.3^{+5.3}_{-7.2}$
ζ (km/s)	Macroturbulent Velocity	$4.3^{+2.2}_{-2.5}$	$3.9^{+2.3}_{-2.5}$	$4.8^{+1.3}_{-1.5}$	$14.4^{+1.1}_{-1.1}$	$3.6^{+1.9}_{-2.3}$
β (km/s)	Thermal Velocity	$1.05^{+0.65}_{-0.7}$	$0.504^{+0.34}_{-0.34}$	$1.02^{+0.33}_{-0.35}$	$1.03^{+0.34}_{-0.35}$	$2.07^{+1.4}_{-1.5}$
γ (km/s)	Lorentzian Velocity	$3.79^{+0.55}_{-0.58}$	$3.83^{+0.87}_{-0.92}$	$4.28^{+0.58}_{-0.62}$	$4.73^{+0.21}_{-0.23}$	$0.886^{+0.73}_{-0.71}$
P_{rot} (days)	Rotational Period	$2.85^{+0.12}_{-0.12}$	$5.38^{+0.04}_{-0.04}$	$4.93^{+0.065}_{-0.066}$	$5.18^{+0.13}_{-0.13}$	$6.43^{+0.079}_{-0.079}$
τ_ψ (yr)	Realignment Timescale	2.58×10^5	6.40×10^7	3.60×10^6	2.20×10^7	1.62×10^7
τ_{sync} (yr)	Synchronization Timescale	1.29×10^5	3.20×10^7	1.80×10^6	1.10×10^7	8.10×10^6
$\tau_{\text{circ,A}}$ (yr)	Circularization Timescale (Primary)	1.08×10^8	3.69×10^9	8.28×10^8	3.81×10^8	5.32×10^9
$\tau_{\text{circ,B}}$ (yr)	Circularization Timescale (Secondary)	1.53×10^5	2.92×10^6	1.01×10^6	7.21×10^5	4.56×10^6

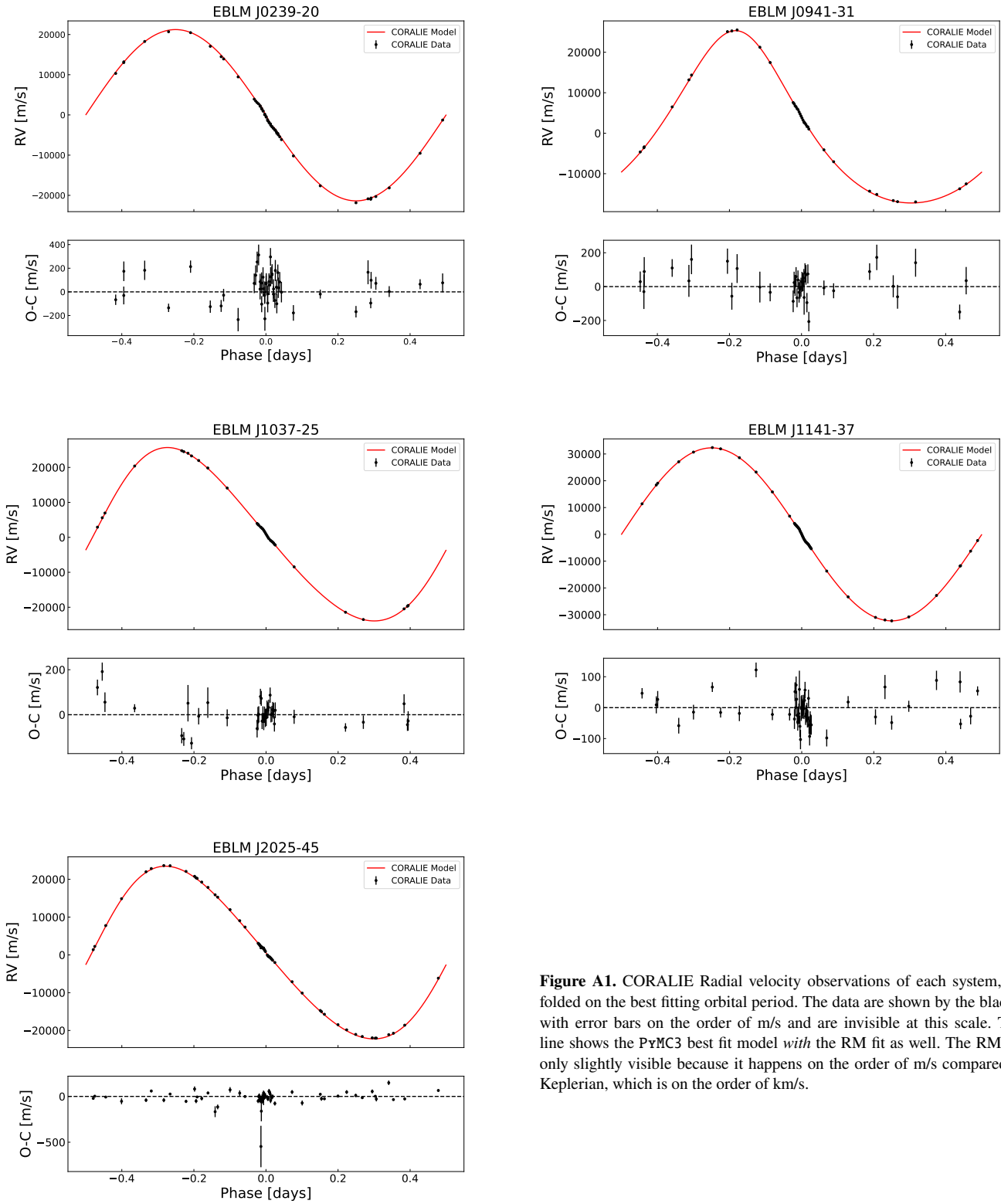


Figure A1. CORALIE Radial velocity observations of each system, phase-folded on the best fitting orbital period. The data are shown by the black dots, with error bars on the order of m/s and are invisible at this scale. The red line shows the PrMC3 best fit model *with* the RM fit as well. The RM here is only slightly visible because it happens on the order of m/s compared to the Keplerian, which is on the order of km/s.

This paper has been typeset from a $\text{\TeX}/\text{\LaTeX}$ file prepared by the author.

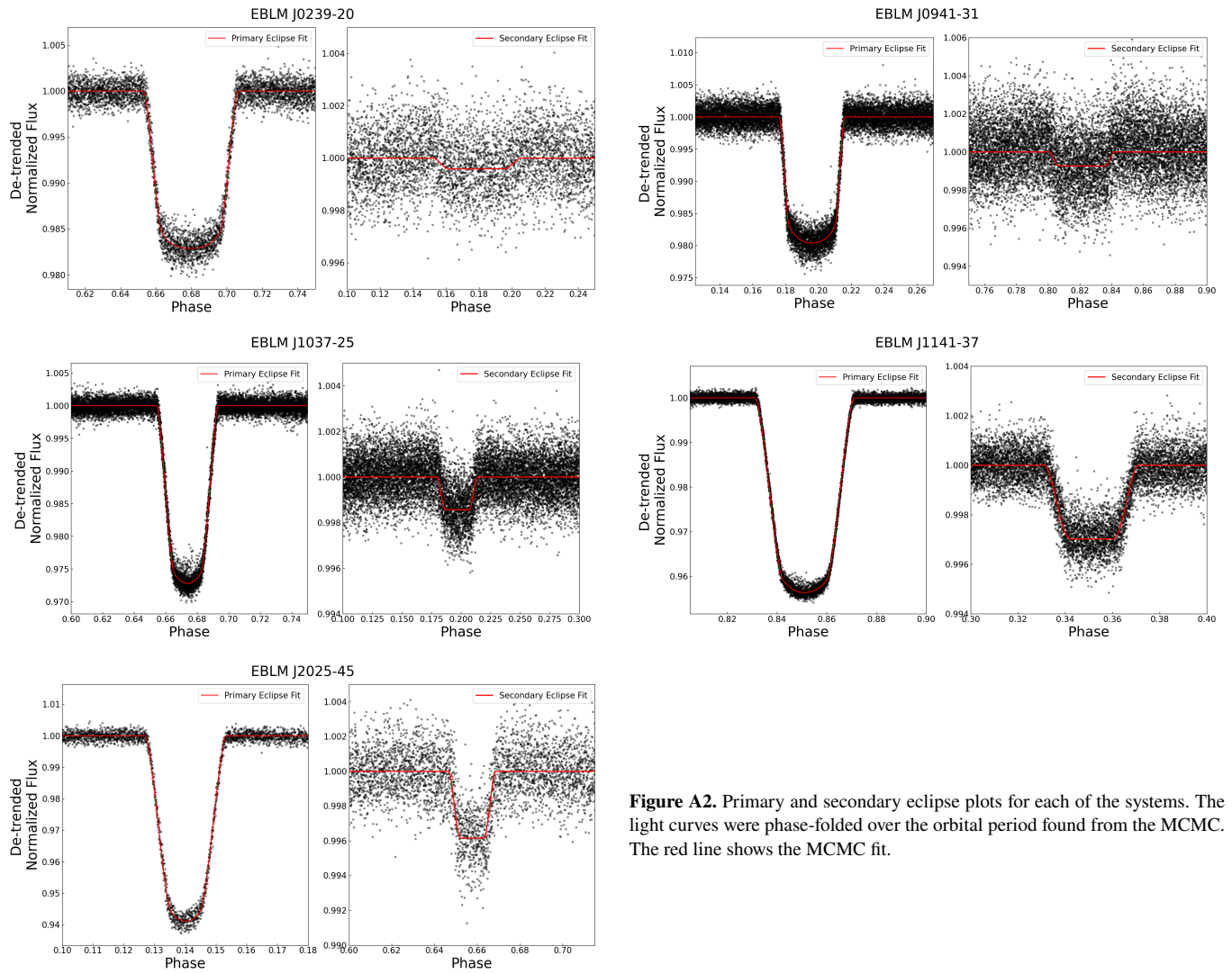


Figure A2. Primary and secondary eclipse plots for each of the systems. The light curves were phase-folded over the orbital period found from the MCMC. The red line shows the MCMC fit.

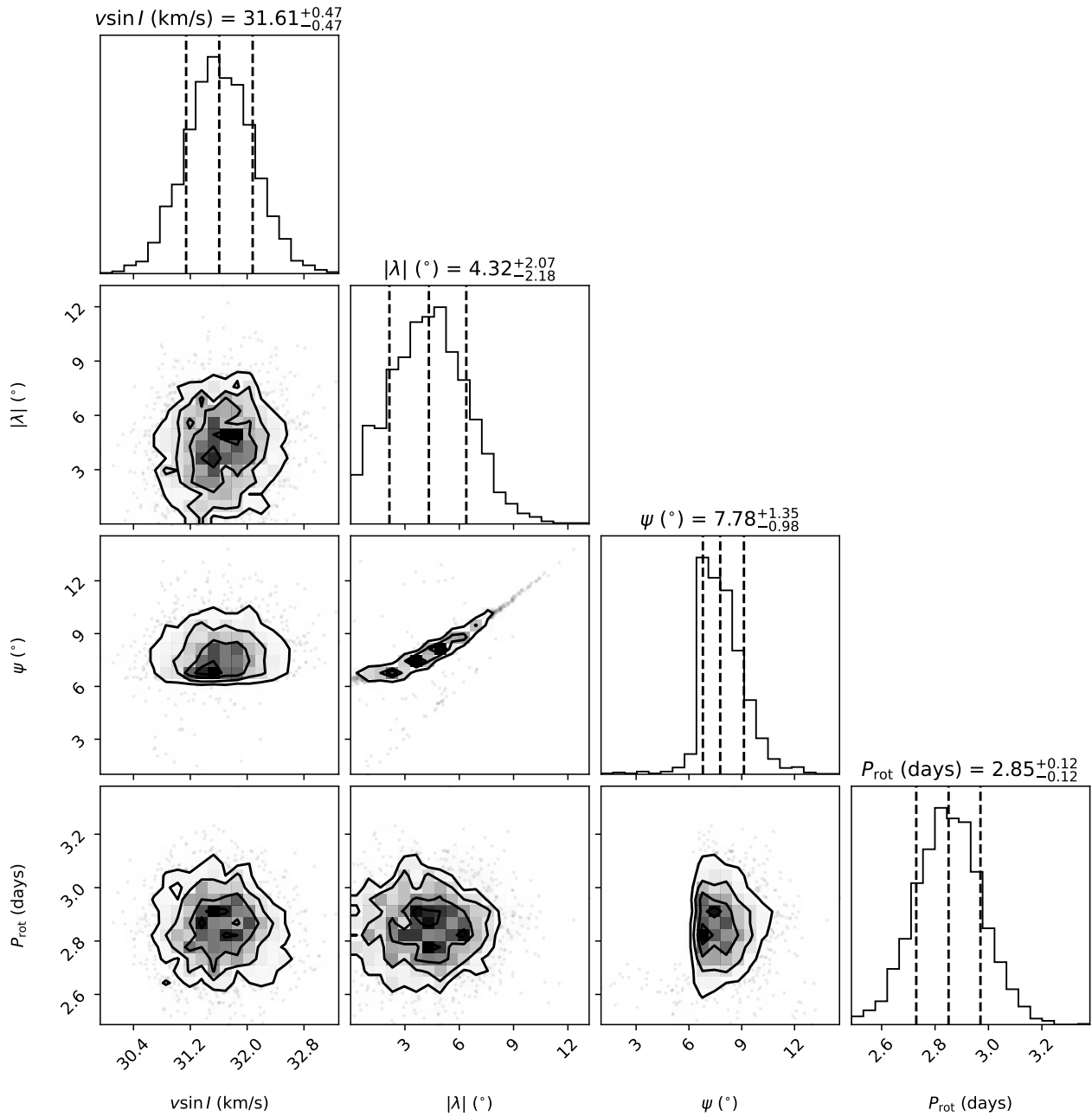


Figure A3. Corner plot for EBLM J0239-20 produced from the MCMC simulation of the joint fit to all RVs (Keplerian and Rossiter) and the TESS photometry for primary and secondary eclipses. The plot shows the correlation between the parameters corresponding to the RM fit - $v_{\text{rot}} \sin I_*$, λ , ψ , & P_{rot} .

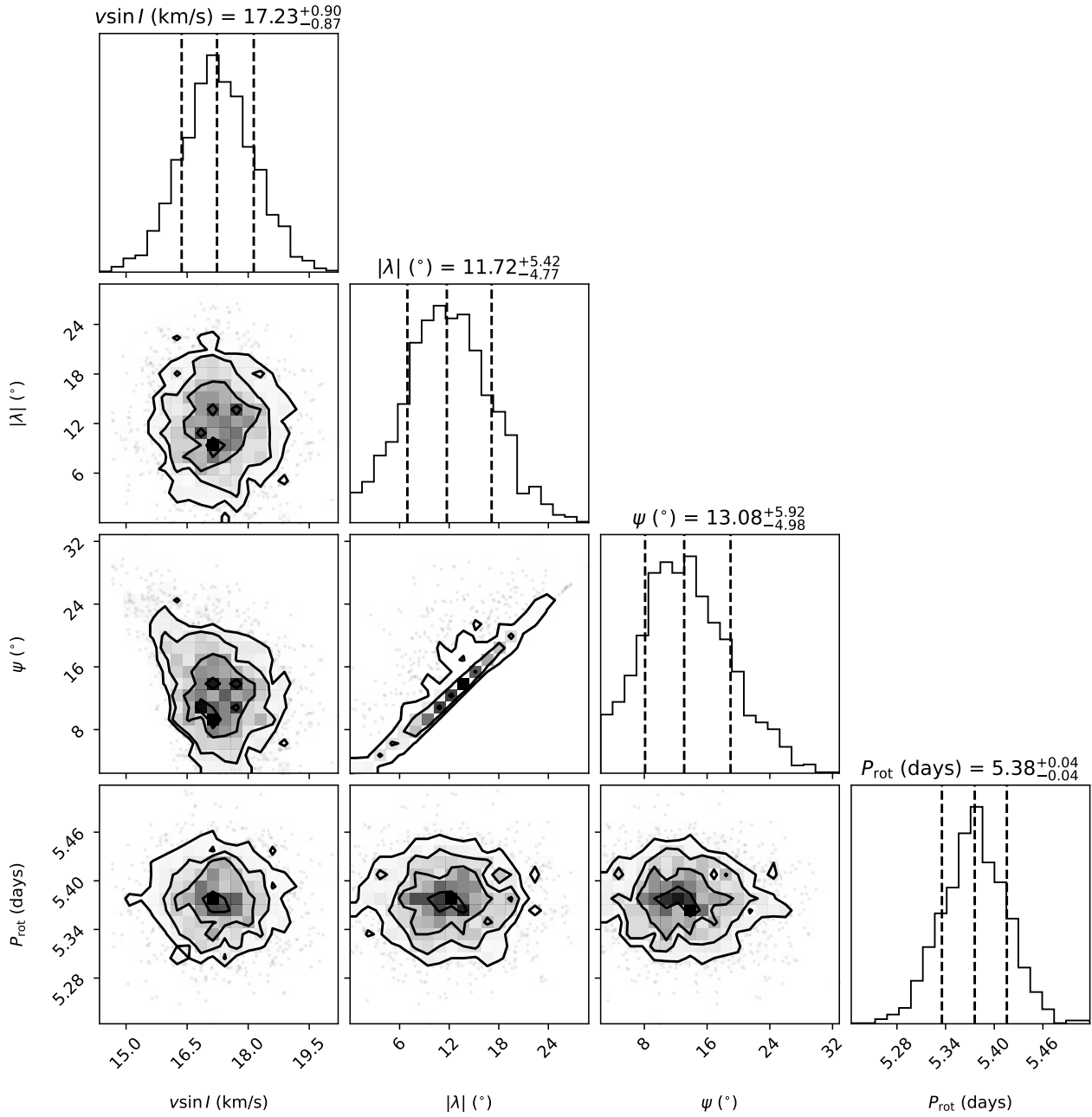


Figure A4. Corner plot for EBLM J0941-31 produced from the MCMC simulation of the joint fit to all RVs (Keplerian and Rossiter) and the TESS photometry for primary and secondary eclipses. The plot shows the correlation between the parameters corresponding to the RM fit - $v_{\text{rot}} \sin I_*$, λ , ψ , & P_{rot} .

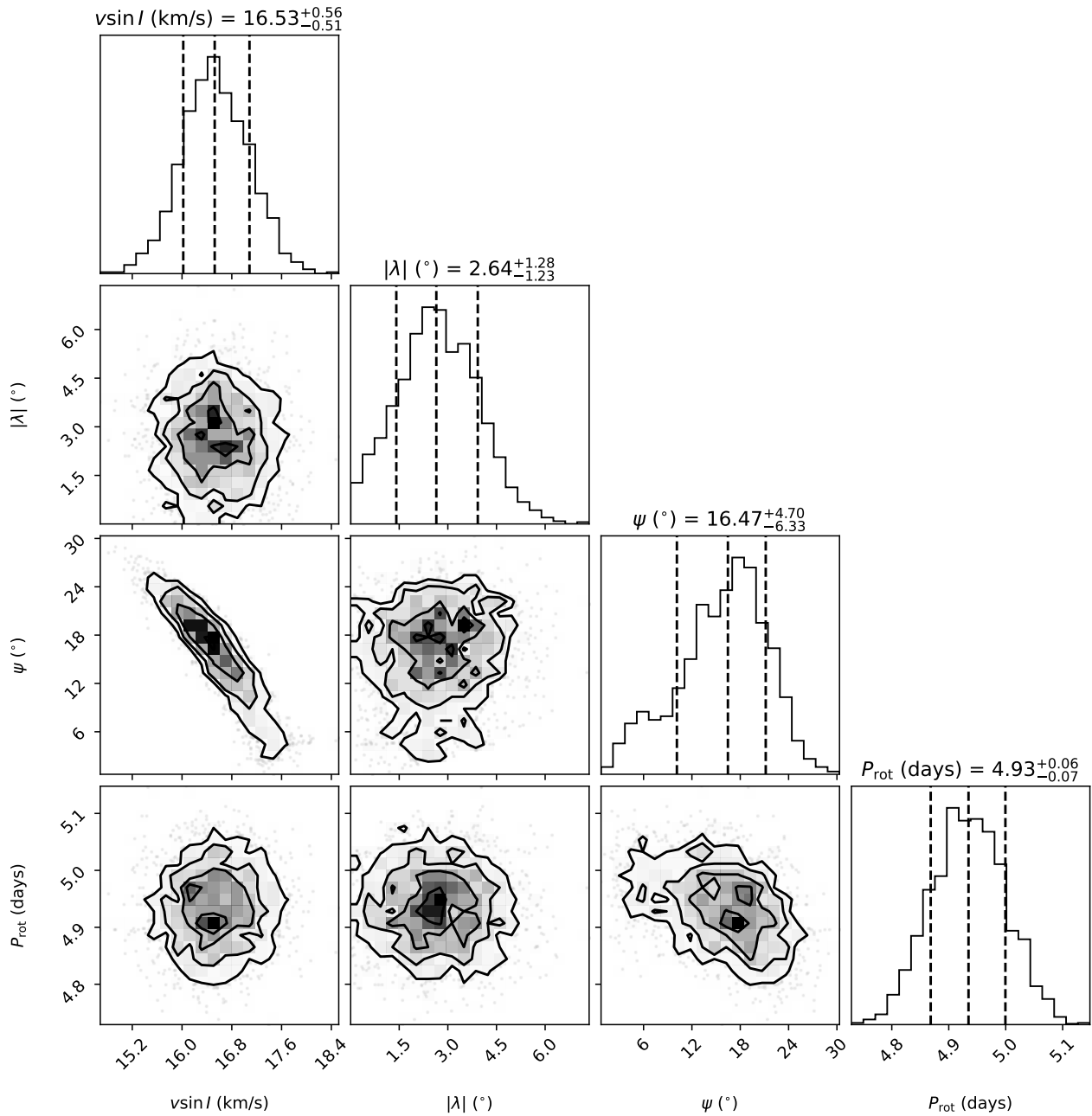


Figure A5. Corner plot for EBLM J1037-25 produced from the MCMC simulation of the joint fit to all RVs (Keplerian and Rossiter) and the TESS photometry for primary and secondary eclipses. The plot shows the correlation between the parameters corresponding to the RM fit - $v_{\text{rot}} \sin I_{\star}$, λ , ψ , & P_{rot} .

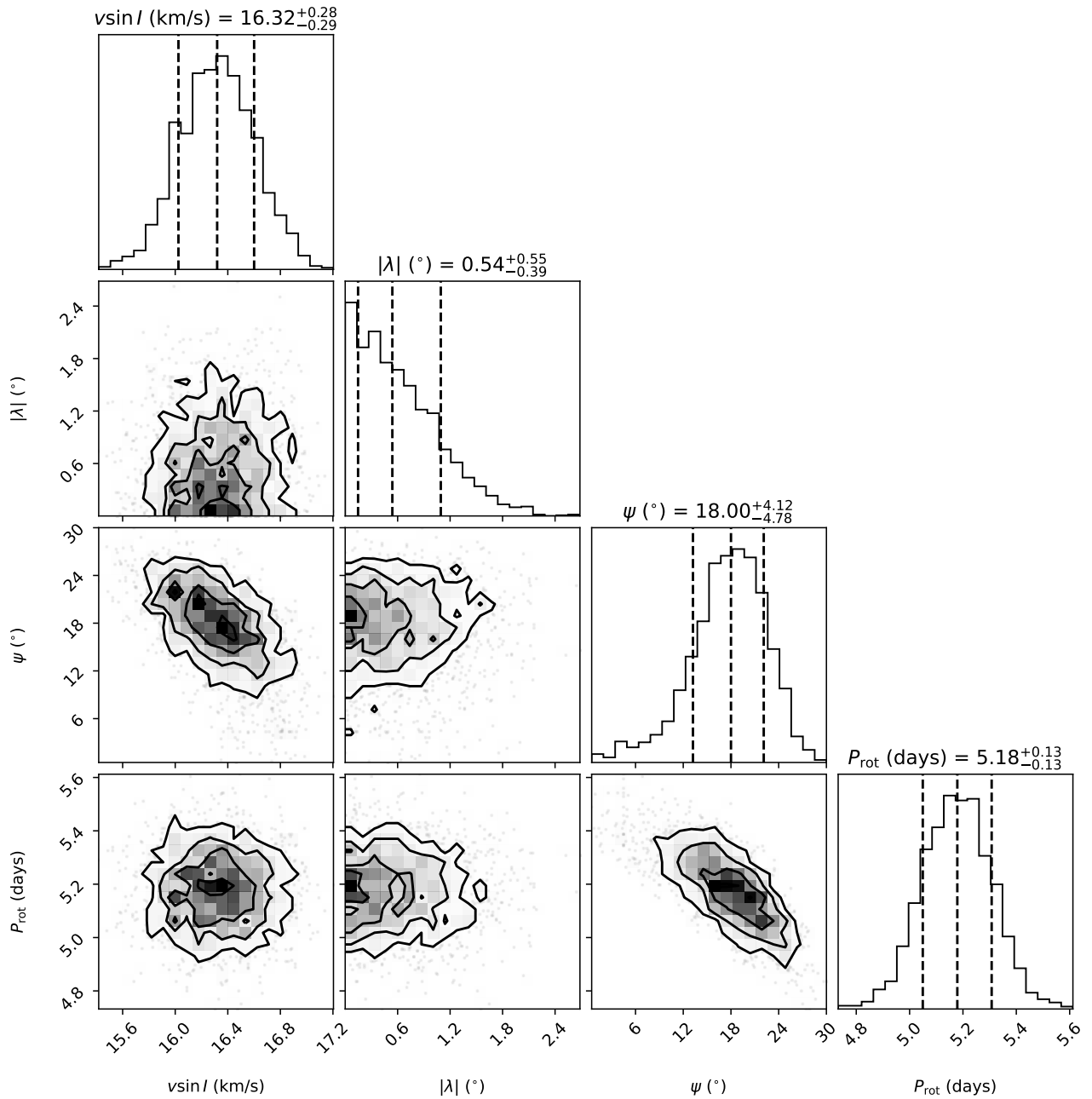


Figure A6. Corner plot for EBLM J1141-37 produced from the MCMC simulation of the joint fit to all RVs (Keplerian and Rossiter) and the TESS photometry for primary and secondary eclipses. The plot shows the correlation between the parameters corresponding to the RM fit - $v_{\text{rot}} \sin I_*$, λ , ψ , & P_{rot} .

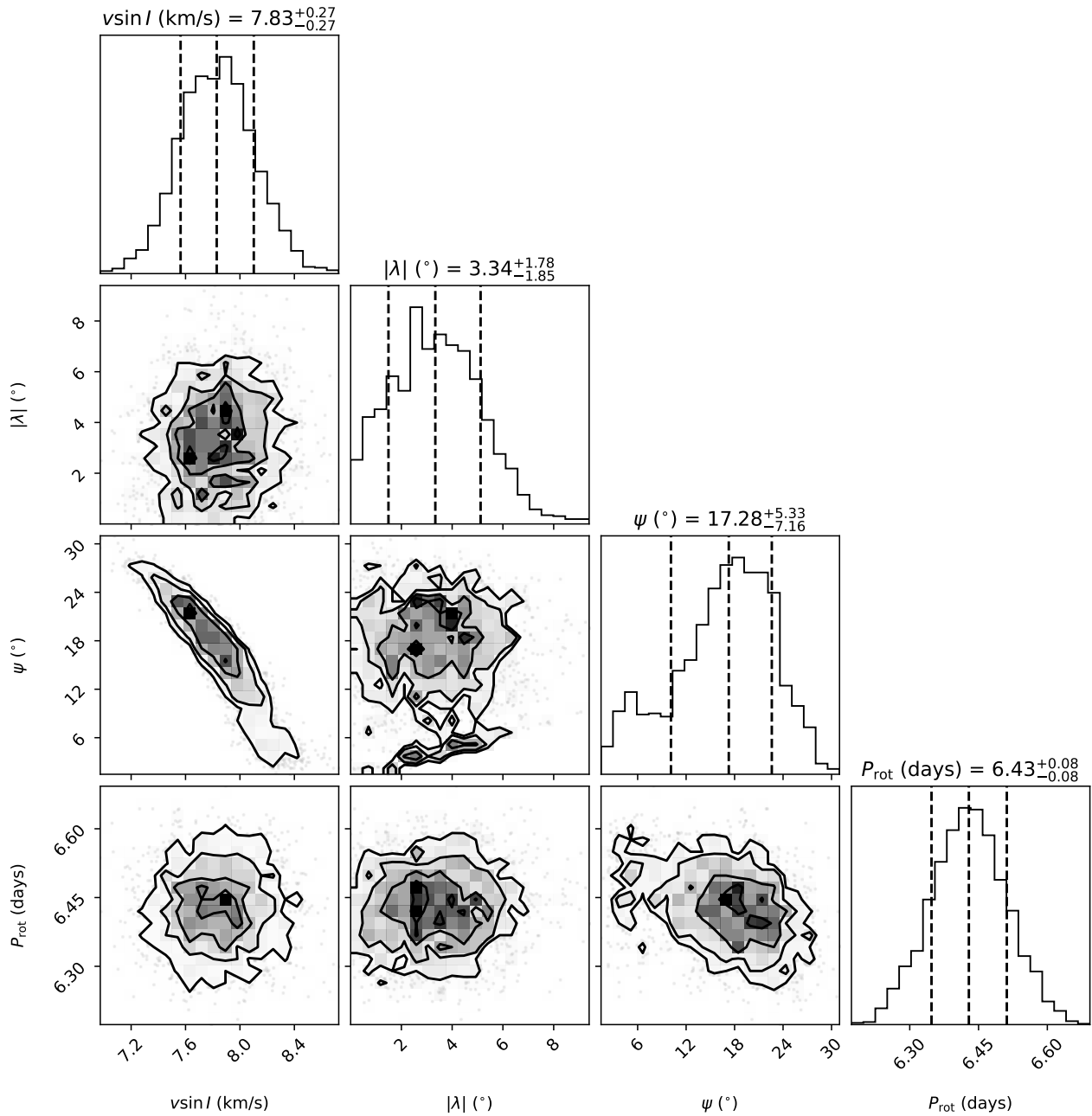


Figure A7. Corner plot for EBLM J2025-45 produced from the MCMC simulation of the joint fit to all RVs (Keplerian and Rossiter) and the TESS photometry for primary and secondary eclipses. The plot shows the correlation between the parameters corresponding to the RM fit - $v_{\text{rot}} \sin I_*$, λ , ψ , & P_{rot} .